

# An Improved Calibration Algorithm for the L-Band 1-D Synthetic Aperture Radiometer

Aili Zhang<sup>\*, 1, 2</sup>, Hao Liu<sup>1</sup>, and Ji Wu<sup>1, 2</sup>

**Abstract**—L-band one-dimensional (1-D) synthetic aperture radiometer is a passive microwave imager that aims to produce global sea surface salinity and soil moisture maps. Two instrument concepts for the L-band 1-D synthetic aperture radiometer have been proposed and selected as candidate payloads for future Chinese space missions, including MICAP (Microwave Imager Combined Active and Passive) for the Chinese Ocean Salinity Mission and IMI (Interferometric Microwave Imager) for the Water Cycle Observation Mission (WCOM). For a synthetic aperture radiometer, spatial imaging error is defined as the difference between the original brightness temperature (BT) and the retrieved BT images within the alias-free field of view (AF-FOV). The main causes of image spatial error in the L-band 1-D system are antenna elements spacing and antenna patterns error. Flat target transformation (FTT) algorithm is always useful for correcting radiometer imaging, but there is still a concave residual error in the retrieved image. An improved calibration algorithm is proposed, which replaces the cold sky view in the FTT with a stable reference scene BT image. A task simulator has been set up to evaluate the new method. The proposed calibration algorithm is shown to reduce the spatial bias and improve the quality of the retrieved BT image.

## 1. INTRODUCTION

Soil moisture and ocean salinity are two main geophysical parameters that play key roles in the global water cycle and climate change. L-band radiometry has been identified as a very effective tool for measuring these two parameters from space. Three space missions with L-band instruments onboard have already been successfully implemented, i.e., the ESA's SMOS mission launched in 2009 with a two-dimensional Y-shape interferometric microwave radiometer called MIRAS [1], NASA's Aquarius mission, which was launched in 2011 with a three-beam push-broom radiometer/scatterometer [2], and the SMAP mission launched in 2015 with a conical scanning radiometer and SAR [3].

In China, a new concept of combining L-band active and passive sensors was proposed by NSSC in 2012. The passive part of this concept is a 1-D interferometric microwave radiometer, while the active sensor is a digital beamforming scatterometer. The active and passive parts are installed together sharing a common parabolic cylinder reflector [4]. NSSC also has developed a ground-based demonstrator during 2012–2015, as shown in Fig. 1, and taken experiments to evaluate the imaging performance including the spatial resolution, stability, and accuracy [5]. The imaging algorithm is also verified through experiments.

For synthetic aperture radiometers, brightness temperature (BT) image is obtained by taking the Fourier transform of the complex cross correlations, i.e., the visibility function can be measured between the received bandpass noises collected by every pair of antenna elements in the array [6]. According to the definition of the visibility function given by Corbella et al., [7], the imperfect performance of the

---

Received 17 February 2019, Accepted 2 April 2019, Scheduled 15 April 2019

\* Corresponding author: Aili Zhang (zhangaili19910128@gmail.com).

<sup>1</sup> Key Laboratory of Microwave Remote Sensing, National Space Science Center, Chinese Academy of Science, Beijing 100190, China.

<sup>2</sup> University of Chinese Academy of Science, Beijing 100049, China.

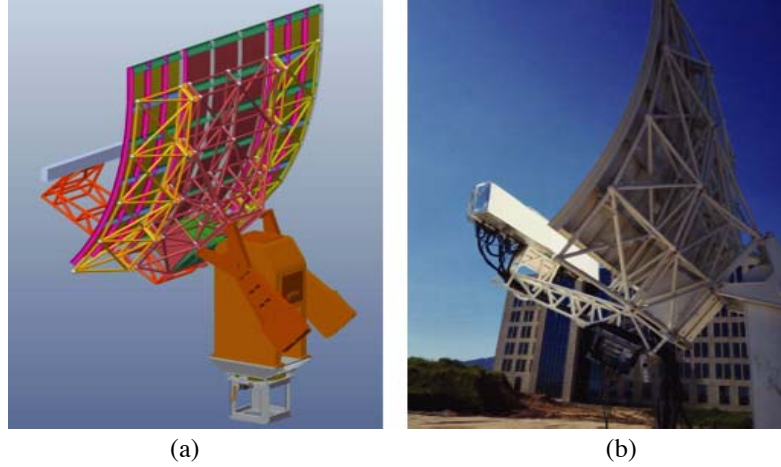


**Figure 1.** (a) Structural view of L-band 1-D synthetic aperture radiometer. (b) Picture of the ground prototype.

radiometer instrument, especially the antenna error, is one of the main causes of imaging error, which is also explained by Diez-Garcia et al. [8]. In order to produce quality geophysical parameter retrievals, the so-called Flat Target Transformation (FTT) algorithm is applied in the BT image reconstruction algorithm in level-1 processor of SMOS to mitigate imaging error [9]. At present, FTT algorithm is the main external calibration algorithm used in the imaging process of synthetic aperture radiometer to calibrate the radiometer antenna pattern error. FTT is based on Corbella equation. In Corbella equation, the amplification factor of antenna error is the difference between the target scene brightness temperature and receiver physical temperature. In FTT algorithm, this amplification factor is changed as the difference between the target scene brightness temperature and its mean value. In practical applications, the former is much larger than the latter. Therefore, FTT algorithm is a robust method to calibrate the antenna error. In order to further reduce the amplification factor of the antenna error, a Reference Target Transformation (RTT) algorithm is also proposed to reduce the spatial bias in the process of the BT image reconstruction from the visibility samples, resulting in cleaner BT data.

## 2. IMAGING PRINCIPLE OF SYNTHETIC APERTURE RADIOMETER

The observation measurement of the radiometer is the process of visibility function sampling. The BT image reconstruction is the BT image retrieval from the observed data. Considering the weighting function of the antenna pattern, the samples of the visibility function can be expressed as Eq. (1). For classical interferometric synthetic aperture radiometry, the samples of the visibility function are given by [10, 11],

$$V_{i,j}(u, v) = \iint_{\xi^2 + \eta^2 \leq 1} \frac{T_B(\xi, \eta)}{\Omega_{eq} \sqrt{1 - \xi^2 - \eta^2}} F_i(\xi, \eta) F_j^*(\xi, \eta) \tilde{r}_{i,j}(\tau) e^{-j2\pi(u\xi + v\eta)} d\xi d\eta$$

$$\tau = -\frac{u\xi}{f}, u = \frac{L}{\lambda} \quad (1)$$

where  $F(\xi, \eta)$  is the normalized antenna voltage pattern, which is a complex function including amplitude and phase.  $T_B(\xi, \eta)$  is the BT value of observational target scene.  $\tilde{r}_{i,j}$  is the so-called fringe-washing function, which accounts for spatial decorrelation effects and depends on the frequency response of the pair of elements collecting the signals being correlated.  $V_{i,j}$  is the sampled visibility function.  $L$  is the spacing between the  $i$ -th antenna element and  $j$ -th antenna element.  $\xi$  and  $\eta$  are the direction cosine coordinates,  $\xi = \cos\phi \sin\theta$ , and  $\eta = \sin\phi \sin\theta$ , where  $\phi$  and  $\theta$  are the azimuth and height angles, respectively.  $f$  is the operating frequency of the radiometer system. Since this radiometer is a 1-D system, Equation (1) can be expressed as a 1-D function when considering  $\xi = 0$  and  $v = 0$ .

In practical applications, the mutual coupling between antenna elements must be included in the visibility function, so the BT term in Equation (1) is replaced by  $T_B(\xi, \eta) - T_r$ . Equation (1) is modified as:

$$V_{i,j}(u, v) = \iint_{\xi^2 + \eta^2 \leq 1} \frac{T_B(\xi, \eta) - T_r}{\Omega_{eq} \sqrt{1 - \xi^2 - \eta^2}} F_i(\xi, \eta) F_j^*(\xi, \eta) \tilde{r}_{i,j}(\tau) e^{-j2\pi(u\xi + v\eta)} d\xi d\eta \quad (2)$$

where  $T_r$  is the physical temperature of the receiver isolator [7]. The value of  $T_r$  is assumed to be 300K in the simulations, and the receiver noise is not included in the current simulations.

Due to the difference between antenna patterns in the 1-D radiometer system, the Inverse Fast Fourier Transform (IFFT) algorithm cannot achieve accurate reconstruction of brightness temperature images. Referring to the ESTAR's experience, then, the G-matrix method based on numerical inversion is used to reconstruct the BT map. Equations (1) and (2) can be discretized into a set of linear equations, and expressed as a matrix function

$$V_{K \times 1} = G_{K \times P} T_{B_{P \times 1}} \quad (3)$$

where " $G_{K \times P}$  matrix" characterizes the linear relationship between the visibility samples and target scene BT image [12].  $K = 2 \times M + 1$ , where  $M$  refers to the number of continuous non-redundant baselines. When considering the conjugate symmetry and zero-baseline, the total number of visibility samples is  $K$ . The size of 2-D scene brightness temperature map is set to  $P = N \times N$ . Now, the set of visibility samples can be combined in the matrix equation

$$\begin{bmatrix} V_1 \\ V_2 \\ V_3 \\ \vdots \\ V_K \end{bmatrix} = \begin{bmatrix} AP_1(\xi_1, \eta_1) e^{-j2\pi u_1 \xi_1} & \dots & AP_1(\xi_N, \eta_N) e^{-j2\pi u_1 \xi_N} \\ \vdots & \ddots & \vdots \\ AP_K(\xi_1, \eta_1) e^{-j2\pi u_K \xi_1} & \dots & AP_K(\xi_N, \eta_N) e^{-j2\pi u_K \xi_N} \end{bmatrix} \times \begin{bmatrix} T_B(\xi_1, \eta_1) \\ \vdots \\ T_B(\xi_N, \eta_1) \\ \vdots \\ T_B(\xi_1, \eta_N) \\ \vdots \\ T_B(\xi_N, \eta_N) \end{bmatrix} \quad (4)$$

where  $AP_K = F_i(\xi, \eta) F_j^*(\xi, \eta)$  is the conjugate product of a pair of antenna patterns on the  $k$ -th baseline. In practical applications, especially for a radiometer system with a small number of antenna elements, since  $P$  is greater than  $K$ ,  $G$  has no unique inverse. Consequently, the Moor-Penrose pseudoinverse method can be used as the inversion algorithm and reach a good reconstruction result for a small-size synthetic aperture radiometer system [13]. For example, in the ground radiometer prototype with 8-element linear feed array, there are only 18 continuous non-redundant visibility samples, which results in a small-size  $G$  matrix. Therefore, the image reconstruction algorithm used in this paper is the Moore-Penrose pseudo-inverse algorithm, as shown in Equation (5).

$$\widehat{T}_B = G^+ V = G^H (G G^H)^{-1} V \quad (5)$$

where  $\widehat{T}_B$  is the retrieved BT image, and  $G^+$  is the pseudoinverse matrix of matrix. The G-matrix method combining image retrieval and error calibration is well suitable for a 1-D synthetic aperture radiometer system [13].

### 3. SPATIAL IMAGING ERROR

The visibility samples are measured by the L-band 8-element 1-D synthetic aperture radiometer during the observation of the BT image, as shown in Fig. 2. The image spatial error is defined by the difference between the original BT image of the target scene and the retrieved BT image. According to the definition of the visibility function in Eqs. (1) and (2), the imperfections, differences in antenna patterns, and antenna spacing have impacts on the radiometer's image reconstruction. The  $T_B(\xi, \eta) - T_r$  term in Eq. (2) is a multiplicative factor of antenna pattern and is the amplification factor of antenna error.

The minimum antenna spacing ( $\Delta u$ ) of the 1-D synthetic aperture interferometric radiometer is  $0.6125\lambda$ , which is larger than 0.5 and then inevitably causes aliasing effect in the retrieved image. The aliasing free Field of View (AF-FOV) defined in the unit circle is shown in Fig. 2, where the Earth

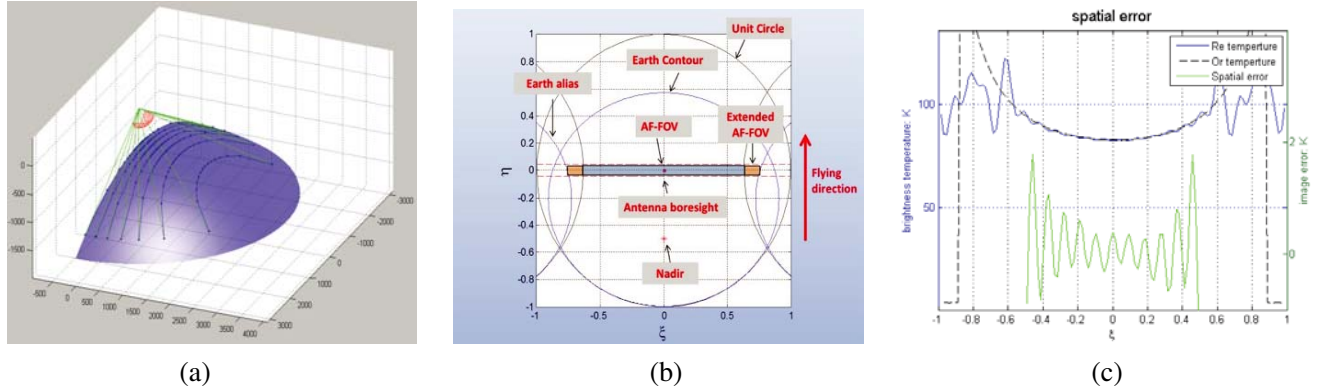


**Figure 2.** (a) Illustration of the process to observe the earth. (b) Aliasing in the 1-D synthetic aperture interferometric radiometer for an antenna spacing of 0.6125 wavelengths, and 657-km platform height. Representation of the Earth’s disk (Earth-sky horizon). (c) Target scene BT image (the observational image) (black curve), Retrieved BT image (blue) and image error (green) from 1-D radiometer simulation.

contour and the extended AF-FOV caused by the cold sky are also illustrated. The width of the alias-free field of view is approximately  $[-0.625 + 0.625]$ . The H-polarized image retrieval results of the ocean scene are shown in Fig. 2, where the black dashed curve denotes the original BT image of the target scene; the blue curve denotes the retrieved BT image; and the green curve denotes the retrieval error, within the AF-FOV. The Blackman function is applied in the simulations.

## 4. CALIBRATION ALGORITHMS

### 4.1. The Flat Target Transformation

The FTT algorithm is an overall calibration algorithm proposed by Corbella et al. [9], which is used to calibrate the spatial imaging error in the SMOS mission. The Flat Target Response (FTR) can be obtained by looking at the cold sky near the galactic poles. The essence of FTT is to change the magnification factor of antenna error,  $T_B(\xi, \eta) - T_r$ , to the difference between observational target scene BT and its mean value, thus reducing the impact of the antenna pattern error. The reference temperature in the FTT algorithm is defined as the average brightness temperature over all pixels in the field of view. An alternative exists in the choice of the FTT reference temperature, as shown in Fig. 3, where the imaging error (RMS) gradually changes with the reference temperature for the ocean scene observation. In the simulation experiment, the antenna amplitude and phase uncertainty errors are 1%

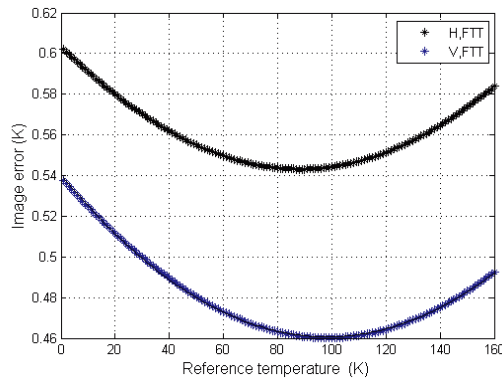


**Figure 3.** Image error as a function of the FTT reference temperature. The image errors evaluated in the H-pol as well as the V-pol are respectively shown as black and the blue curves.

and  $1^\circ$ , respectively. The simulation results indicate that the FTT method has better performance of correcting the antenna pattern error when the reference temperature approaches the average scene BT values. Since the image error is dependent on the polarization mode, it makes sense to use the mean value of the two polarized BT values as the reference temperature desired to minimize the impact of antenna errors. At present, the FTT algorithm has been applied to the simulation experiments and field observation experiments of the ground prototype.

#### 4.2. Reference Target Transformation (RTT)

The reference temperature  $\bar{T}_B$  of the FTT algorithm is the average value over all pixels in the FOV. The BT image of the target scene changes with the direction cosines  $(\xi, \eta)$  in the whole FOV. Therefore, there is still a residual non-zero bias in the factor  $T_B(\xi, \eta) - \bar{T}_B$ . The influence of antenna errors on image retrieval is still magnified by this residual difference. Therefore, a residual image error is still present due to this imperfection of the FTT methodology related to the angular variation of the ocean  $T_B(\xi, \eta)$  [14].

In order to reduce the residual concave difference between the target scene BT image  $T_B(\xi, \eta)$  and reference temperature  $\bar{T}_B$ , an improved calibration algorithm RTT is proposed to observe a reference stable ocean scene BT image  $T_{R\_model}$  instead of the cold sky view. Fig. 4 shows a flowchart of the RTT-based image reconstruction process.

In this case, the retrieved BT image in the process of image reconstruction is represented as follows:

$$\hat{T}_B = G^+(V_{target} - V_{reference}) + T_{R\_model} \tag{6}$$

where  $G^+$  denotes the pseudoinverse matrix of  $G$  matrix.  $G$  matrix denotes the matrix computed from the measured antenna patterns, which is used to reconstruct the image.  $V_{reference}$  is simulated measurements of the reference scene visibility samples. In order to reasonably evaluate the correction effect of the RTT algorithm on the antenna pattern errors, we should distinguish the difference between

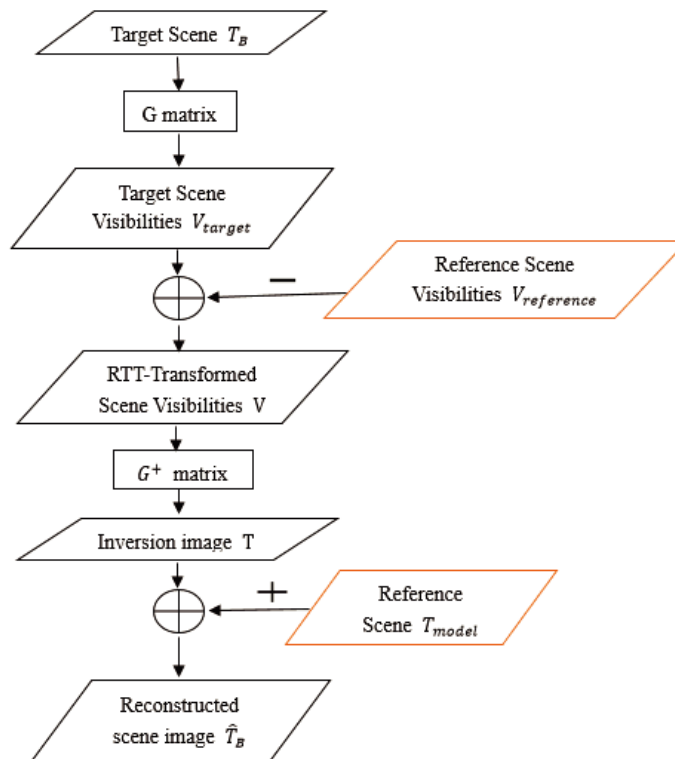


Figure 4. Flowchart of the image reconstruction based on the RTT algorithm.

the  $G$  matrix used to reconstruct the image and the  $G'$  matrix used to generate  $V_{reference}$ . Therefore, when the reference scene BT image is modeled correctly, the simulated measurements of the reference scene visibilities can be described as

$$V_{reference} = G' T_{R\_model} \quad (7)$$

$$G' = G + \Delta G \quad (8)$$

where  $G'$  matrix refers to the instrument observation matrix. The difference  $\Delta G$  denotes the deviation in the  $G$  matrix due to the instrument errors, including the antenna pattern errors.

$T_{R\_model}$  is the modeled reference scene BT image. The selection of the reference scene in the RTT algorithm is critical, and the ocean scenes where the BT images can be accurately modeled should be selected.

The RTT algorithm is more suitable for the observation of an ocean scene, since the accurate modeling of the reference scene BT image is easy to implement, because the target scene is relatively homogeneous and stable. The modeling accuracy of the reference scene BT image is a main factor that directly affects the accuracy of the RTT algorithm to calibrate the image spatial error.

In practice, the modeled reference scene BT image  $T_{R\_model}$  is obtained by using geophysical parameters such as sea surface temperature, wind velocity, salinity, and water vapor content [14]. This process is similar to the establishment of the modeled BT image in OTT algorithm mentioned in salinity retrieval algorithm [15]. In OTT algorithm, the modeled BT image  $T_{model}$  is used to calculate OTTs and to correct the bias in the SMOS L1C data.

In RTT algorithm, the retrieved BT image is computed as Equation (6), and then the retrieved BT image can also be established by

$$\widehat{T}_B = G^+(G'T_B - G'T_{R\_model}) + T_{R\_model} = G^+G'(T_B - T_{R\_model}) + T_{R\_model} \quad (9)$$

In FTT algorithm, the retrieved BT image is

$$\widehat{T}_B = G^+(G'T_B - G'\overline{T}_B) + \overline{T}_B = G^+G'(T_B - \overline{T}_B) + \overline{T}_B \quad (10)$$

In an ideal case, there is no any instrument error,  $G' = G$  and  $G^+G' = 1$ . The reconstructed images obtained by FTT and RTT both are the real brightness temperature of the target scene. However, in practical applications,  $\Delta G \neq 1$  and  $G^+G' \neq 1$ , the term  $G^+G'$  contains the antenna pattern errors and other instrument errors. Equation (10) shows that the antenna error is amplified by the factor  $T_B - \overline{T}_B$  in FTT algorithm, while Equation (9) shows the amplification factor has been changed to  $T_B - T_{R\_model}$  in RTT algorithm. Therefore, the amplification factor has been significantly reduced in RTT algorithm as  $T_B - T_{R\_model}$  is always smaller than  $T_B - \overline{T}_B$  in the open and stable ocean.

### 4.3. FTT and RTT Simulation Experiments

Full functional simulations are implemented to evaluate the influence of antenna errors and validate the calibration algorithms. The antenna patterns used in the next simulation are the measured patterns of the ground prototype. In order to simulate the antenna pattern uncertainty errors, random ripple errors with amplitude uncertainty  $\sigma_{pattern\_ampli} = 1\%$  and random ripple phase uncertainty  $\sigma_{pattern\_phase} = 1^\circ$  are introduced to the measured antenna patterns to generate the contaminated matrix  $G'$ . The simulation results based on the three different image reconstruction equations (No FTT, FTT, and RTT) are shown in Fig. 5. Since the antenna pattern error is random, the simulation results in Fig. 5 are not unique. The statistical results of the simulation experiment are listed in Table 1.

The simulation results shown in Fig. 5 clearly demonstrate the advantages of the two calibration approaches. The FTT algorithm used in SMOS mission can effectively calibrate the radiometer system

**Table 1.** Statistical parameters of the simulation.

	NO FTT	FTT	RTT
RMSE(K)	1.0936	0.2683	0.1017
Std(K)	0.9831	0.2559	0.0686

imaging error. The RTT calibration algorithm can further reduce the concave shaped spatial bias error under the condition that the modeled reference ocean-scene BT image  $T_{model}$  is accurate enough.

Combining the orbit design parameters of the spacecraft, a series of scenes observed by the radiometer scanning one track were selected to simulate and evaluate the imaging quality. The ripple antenna uncertainty error,  $\sigma_{pattern\_ampli} = 1\%$  and  $\sigma_{pattern\_phase} = 1^\circ$ , is also assumed in this simulation experiment. The simulation results of the image spatial bias before and after applying FTT and RTT calibration algorithms are shown in Fig. 6. Comparing the above simulation results, it can be concluded that RTT is a more effective calibration algorithm. This conclusion is also consistent with the simulation results of the pure ocean scene observation in Fig. 5.

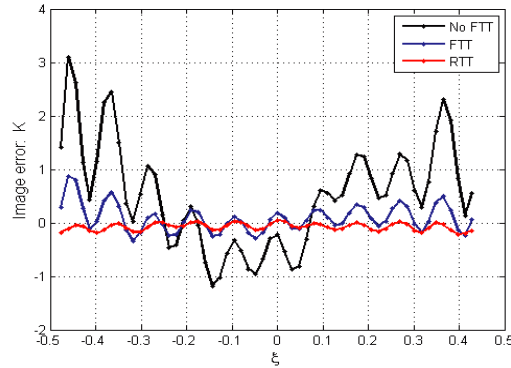


**Figure 5.** Simulation and correction results of a random antenna pattern error, which are based on the three equations, including No FTT, FTT and RTT.

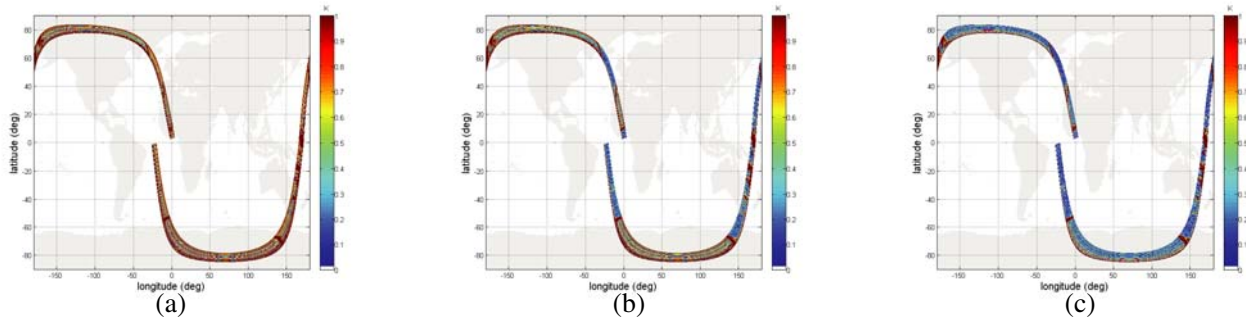


**Figure 6.** (a) The effect of antenna pattern errors on the retrieved brightness temperature image. (b) and (c) respectively represent the image errors from antenna pattern errors calibrated by the FTT and RTT algorithms.

## 5. CONCLUSION

For an L-band 1-D synthetic aperture microwave radiometer system, antenna pattern is an important factor that influences the imaging quality. Many practical factors may bring uncertainties to the knowledge of antenna patterns, such as imperfections in the deployment accuracy of the reflector, imperfections in the mounting accuracy of the antenna feeds, and on-ground chamber measurement limitations. The FTT algorithm given by SMOS mission can effectively reduce image spatial bias, which has been successfully validated by the simulations and field experiments. In this paper, an RTT calibration algorithm is also proposed, which can further reduce the image spatial bias caused by antenna pattern error compared to FTT. The effectiveness of the improved algorithm depends greatly on the accuracy of the modeling of the reference scene BT image. Optimizing the accuracy of the forward model is a major issue of ongoing research.

## ACKNOWLEDGMENT

The authors would like to thank AMSR-E for providing the monthly average data of the meteorological data including sea surface temperature, wind speed, liquid water content, water vapor content in June 2011, and WOA for providing the monthly mean salinity data. The authors are also very grateful for the support of the pre-study programs of WCOM (Water Cycle Observation Mission) and also COSM (Chinese Ocean Salinity Mission).

## REFERENCES

1. Corbella, I., "TMIRAS calibration and performance: Results from the SMOS in-orbit commissioning phase," *IEEE Transactions on Geoscience and Remote Sensing*, Vol. 49, No. 9, 3147–3155, 2011.
2. Vine, D. M. L., "Aquarius: An instrument to monitor sea surface salinity from space," *IEEE Transactions on Geoscience and Remote Sensing*, Vol. 45, No. 7, 2040–2050, 2007.
3. Piepmeier, J. R., "SMAP L-band microwave radiometer: Instrument design and first year on orbit," *IEEE Transactions on Geoscience and Remote Sensing*, Vol. 55, No. 4, 1954–1966, 2017.
4. Liu, H., X.Zhang, L. Niu, et al., "A combined L-band synthetic aperture radiometer and fan-beam scatterometer for soil moisture and Ocean salinity measurement," *2012 IEEE International Geoscience and Remote Sensing Symposium (IGARSS)*, 4644–4647, Munich, 2012.
5. Niu, L., L. Hao, W. Lin, et al., "Experimental study of an L-band synthetic aperture radiometer for ocean salinity measurement," *2016 IEEE International Geoscience and Remote Sensing Symposium (IGARSS)*, 418–421, Beijing, 2016.
6. Camps, A., M. Vall-Llossera, I. Corbella, et al., "Improved image reconstruction algorithms for aperture synthesis radiometers," *IEEE Transactions on Geoscience and Remote Sensing*, Vol. 46, No. 1, 146–158, 2008.
7. Corbella, I., N. Duffo, et al., "The visibility function in interferometric aperture synthesis radiometry," *IEEE Transactions on Geoscience and Remote Sensing*, Vol. 42, No. 8, 1677–1682, 2004.
8. Diez-Garcia, R. and M. Martin-Neira, "Antenna spacing and pattern differences: Their impact in MIRAS reconstruction error," *2016 14th Specialist Meeting on Microwave Radiometry and Remote Sensing of the Environment (MicroRad)*, 19–24, Espoo, 2016.
9. Martin-Neira, M., M. Suess, J. Kainulainen, et al., "The flat target transformation," *IEEE Transactions on Geoscience and Remote Sensing*, Vol. 46, No. 3, 613–620, 2008.
10. Corbella, I., A. Camps, and F. Torres, "Analysis of noise-injection networks for interferometric-radiometer calibration," *IEEE Transactions on Microwave Theory and Techniques*, Vol. 48, No. 4, 545–552, 2000.
11. Moreno-Galbis, P., J. Kainulainen, and M. Martin-Neira, "Experimental demonstration of the Corbella equation for aperture synthesis microwave radiometry," *IEEE Transactions on Geoscience and Remote Sensing*, Vol. 45, No. 4, 945–957, 2007.
12. Tanner, A. B. and C. T. Swift, "Calibration of a synthetic aperture radiometer," *IEEE Transactions on Geoscience and Remote Sensing*, Vol. 31, No. 1, 257–267, 1993.
13. Corbella, I., F. Torres, et al., "Brightness-temperature retrieval methods in synthetic aperture radiometers," *IEEE Transactions on Geoscience and Remote Sensing*, Vol. 47, No. 1, 285–294, 2009.
14. Gourrion, J., R. Sabia, M. Portabella, et al., "Characterization of the SMOS instrumental error pattern correction over the ocean," *IEEE Geoscience and Remote Sensing Letters*, Vol. 9, No. 4, 793–797, 2012.
15. Yin, X., J. Boutin, and P. Spurgeon, "Biases between measured and simulated SMOS brightness temperatures over ocean: Influence of sun," *IEEE Journal of Selected Topics in Applied Earth Observations and Remote Sensing*, Vol. 6, No. 3, 1341–1350, 2013.